Optimal quantum control for conditional rotation of exciton qubits in semiconductor quantum dots

Reuble Mathew,[1] Craig E. Pryor,[2] Michael E. Flatté,[2] and Kimberley C. Hall[1]
[1]*Department of Physics and Atmospheric Science, Dalhousie University, Halifax, Nova Scotia, Canada B3H4R2*
[2]*Department of Physics and Astronomy and Optical Science and Technology Center, University of Iowa, Iowa City, Iowa 52242, USA*
(Received 7 August 2011; revised manuscript received 11 October 2011; published 17 November 2011)

Pulse-shaping protocols for subpicosecond optically controlled quantum gates in semiconductor quantum dots are reported. Our emphasis is the development of shaping schemes for either amplitude or phase control of the pulse that are easily implemented using commercial pulse shapers and femtosecond laser systems. We illustrate the efficacy of our approach through simulations of a controlled-rotation gate in a realistic In(Ga)As quantum dot with electronic structure calculated using eight-band, strain-dependent $\boldsymbol{k}\cdot\boldsymbol{p}$ theory. Our results show that amplitude- and phase-shaping protocols both lead to substantial improvements in fidelity when compared with transform-limited pulses with equivalent gate times. Dephasing was found to have a minimal effect on the gate fidelities due to the ultrafast time scale of the quantum operations.

DOI: 10.1103/PhysRevB.84.205322 PACS number(s): 03.67.Lx, 78.67.Hc

I. INTRODUCTION

The pursuit of quantum control in semiconductor quantum dots (QDs) has been the focus of a considerable body of research over the past decade.[1] In addition to enabling fundamental research into light-matter interactions, in which the three-dimensional quantum confinement provides atomiclike properties in a solid-state environment,[2] semiconductor QDs may become the future building blocks of a quantum computing architecture. Fundamental qubits in individual quantum dots may be realized using the quantum states of an exciton or individual carrier spin.[3–13] Proposals in which optical excitation may be used for both single-qubit rotations and two-qubit gates[4–13] are especially attractive as the exploitation of established semiconductor and photonic device fabrication capabilities enhances the potential for scaling the architecture to a large number of qubits as well as integrating it with existing computing technology. Furthermore, the use of short optical pulses may lead to operating speeds in the THz range. Seminal demonstrations of coherent optical control in QDs in recent years include single-qubit rotations involving excitons,[14–18] biexcitons,[19,20] and single carrier spins,[21,22] as well as quantum state tomography,[23] the coherent manipulation of an exciton spin superposition state,[24] and the introduction of controllable entanglement between excitons.[25–27] (For a recent review, see Ref. 1.) These advancements represent a powerful toolkit for implementations of quantum hardware based on semiconductor QDs.

All of the above demonstrations of coherent optical control utilized transform-limited (TL) optical pulses, for which the phase of the pulse is constant.[28] By harnessing the power of femtosecond pulse-shaping techniques,[29] which allow full control over the temporal dependence of the amplitude and phase of the pulse, one may achieve a much greater degree of flexibility in the manipulation of the quantum state. In recent years, pulse shaping has been applied to quantum control in atomic and molecular systems,[30–35] in the control of chemical reactions,[36,37] and in various areas of nonlinear optics, including electromagnetically induced transparency[38,39] and the generation of high harmonics.[40–42] The potential utility of pulse shaping in quantum computing is clearly illustrated by various proposals for quantum gates based on adiabatic passage,[10,11,43,44] in which a linear chirp (quadratic time-dependent phase) results in state evolution through an anticrossing, something that was very recently demonstrated involving exciton qubits in self-assembled QDs.[45,46] The implementation of a more general phase profile may greatly benefit the efficiency, fidelity, and speed of quantum state control because the control Hamiltonian itself can be tailored to optimize the physical process involved.[6,8,47,48] For example, in order to avoid unintended dynamics associated with nearby states, optical control has been limited in experiments to pulses with a duration of a few picoseconds or longer (e.g., in Ref. 46, 40 ps pulses were used). The achievement of faster operation speeds using pulse-shaping techniques would allow the full potential of optical control methods for quantum operations to be exploited.

Here we develop general pulse-shaping protocols for optimizing the speed and fidelity of optically controlled quantum gates in self-assembled semiconductor QDs. We focus here on the controlled-rotation (C-ROT) operation involving two exciton qubits in a single QD.[5] The possibility of scaling such a system to qubits within different QDs has been addressed in several recent proposals.[4,9,13,49,50] Exciton qubits are attractive due to the ease and efficiency of quantum state control using optical techniques, and have recently been shown to benefit from dynamical decoupling schemes as a means of reducing the effective decoherence rate.[51–53] The C-ROT gate provides a test case that illustrates the effectiveness of the pulse-shaping approach in a physical scenario that is readily accessible using current optical techniques.[25] In a recent work by Chen *et al.*,[6] the fidelity of the C-ROT operation was optimized through the use of two phase-locked, transform-limited pulses with independent bandwidth control of each pulse. The implementation of this approach is complicated by the need for two separately optimized, synchronous laser sources, as well as a stabilized Michelson arrangement.[8] Our emphasis here is to develop general amplitude- and phase-shaping protocols that could be easily implemented with a single mode-locked femtosecond oscillator and a standard commercially available pulse shaper.[55] We optimize amplitude-shaping protocols and phase-shaping protocols separately and find that either leads to a substantial enhancement in fidelity in comparison

to transform-limited pulses with an equivalent gate time. Dephasing is found to have a minimal effect on the gate fidelity, even for T_2 times as low as 10 ps, reflecting the benefits of a subpicosecond gate time. Our findings may be easily extended to other optical operations in QDs, including two-photon Rabi rotations of biexcitons,[56] adiabatic passage involving excitons[45,46] or biexcitons,[43] and schemes for dynamical decoupling.[51–53] Further improvement is likely to be possible when the amplitude and phase shape of the pulse are optimized together.

II. CONDITIONAL EXCITON DYNAMICS

The C-ROT operation, originally proposed by Troiani *et al.*,[5] is achieved using the four-level system created by the vacuum ground state ($|00\rangle$), two oppositely polarized exciton states ($|10\rangle$ and $|01\rangle$), and the bound biexciton state ($|11\rangle$), as shown in Fig. 1(a). The single exciton states $|10\rangle$ and $|01\rangle$ represent two qubits in each quantum dot. In self-assembled In(Ga)As QDs, the anisotropic exchange interaction together with a slight elongation of the dot lifts the degeneracy between the single exciton states and leads to linearly polarized optical selection rules, in which $|10\rangle$ and $|01\rangle$ correspond to symmetric and antisymmetric combinations of spin-up and spin-down excitons.[2,57] In Fig. 1(a), Π_x (Π_y) indicates linearly polarized excitation, with the polarization direction along [110] ([1$\bar{1}$0]), corresponding to the long (short) axes of the QD. The exchange splitting (δ) is greatly exaggerated in Fig. 1(a) for clarity: it is typically found to be $\lesssim$0.2 meV in experiments,[58,59] much smaller than the 12 meV bandwidth of the optical control pulses considered here. The biexciton state $|11\rangle$ corresponds to the bound state of two excitons with opposite spin, and occurs at an energy lower than that required to create two single excitons by an amount Δ_b, the biexciton binding energy.

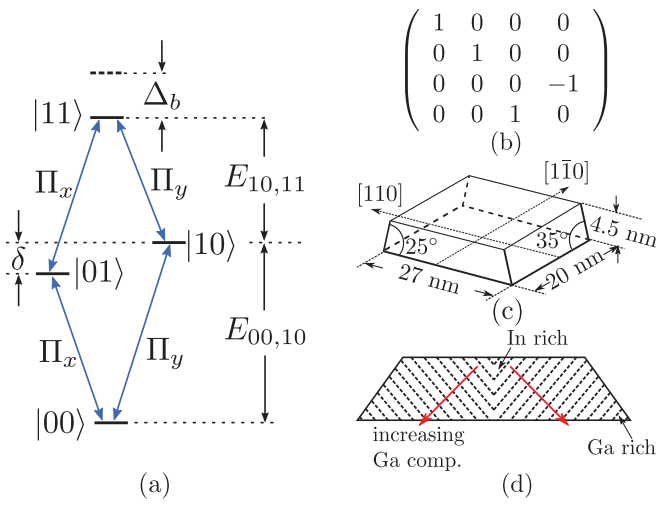

$$\begin{pmatrix} 1 & 0 & 0 & 0 \\ 0 & 1 & 0 & 0 \\ 0 & 0 & 0 & -1 \\ 0 & 0 & 1 & 0 \end{pmatrix}$$

(b)

FIG. 1. (Color online) (a) Energy-level diagram for the exciton and biexciton systems in a QD—the vacuum ground state ($|00\rangle$), two single excitons ($|01\rangle$,$|10\rangle$), and a biexciton ($|11\rangle$) with a binding energy of Δ_b. The arrows indicate optically allowed, linearly polarized (Π_x or Π_y) transitions. (b) Unitary transformation matrix for the C-ROT gate. (c) Truncated pyramid quantum dot structure and (d) $In_xGa_{1-x}As$ composition profile within the dot. The composition is graded from high indium concentration in the shape of an inverted triangle at the center of the dot to low indium concentration at the base.

Conditional dynamics are realized in this system by exploiting the polarization selection rules in Fig. 1(a), in conjunction with the energy separation between the transitions associated with the excitation of a single exciton ($|00\rangle \rightarrow |01\rangle$ or $|10\rangle$) and the excitation of a second exciton in the presence of the first exciton ($|01\rangle$ or $|10\rangle \rightarrow |11\rangle$). These transitions are separated in energy by the biexciton binding energy. Using laser excitation pulses with a spectral bandwidth that is narrow compared to Δ_b, one can achieve both single qubit rotations and a C-ROT gate for suitable choice of the carrier frequency of the laser pulse. For example, for a Π_y-polarized laser pulse tuned to the $|10\rangle \rightarrow |11\rangle$ transition, the state of the second (target) bit will be rotated if and only if the first (control) bit is in state 1. Single qubit rotations (in which a bit is rotated regardless of the state of the other bit) are achieved using bichromatic laser pulses with orthogonally polarized components. The transformation matrix for the C-ROT gate is shown in Fig. 1(b). The restriction to narrow bandwidth excitation pulses ensures a high fidelity operation, but at the expense of a large operation time. As we show in Sec. V, this trade-off between operation time and fidelity may be alleviated through the implementation of pulse shaping.

III. ELECTRONIC STRUCTURE OF SELF-ASSEMBLED QDS

We model the QD as a truncated pyramid of $In_xGa_{1-x}As$ embedded in GaAs, with its base in the (001) plane, and with its edges aligned along the [110] and [1$\bar{1}$0] directions, as shown in Fig. 1(c). The dot has a height of 4.5 nm, a length of 27 nm, and a width of 20 nm, with the long axis along [110]. The facet angles for projections onto the (110) and (1$\bar{1}$0) planes are 35° and 25°, respectively [corresponding to facets with indices of $\{(1,-1,2.020),(-1,1,2.020)\}$ and $\{(1,1,3.033),(-1,-1,3.033)\}$]. We use a graded indium composition within the dot in the shape of an inverted pyramid. The contours in Fig. 1(d) mark nested, constant-alloy composition layers with an angle of 45° to the growth direction. The composition of the dot is graded in 16 increments from the innermost layer at the top face where it is In rich ($x = 0.6$) to the outermost layer at the base where it is Ga rich ($x = 0.225$) (i.e., a change in composition of $\Delta x = 0.025$ between layers). The dot shape and compositional profile is typical of In(Ga)As/GaAs self-assembled QDs.[60–62]

The confined single-particle states of the QD were calculated using an eight-band, strain-dependent $\boldsymbol{k} \cdot \boldsymbol{p}$ Hamiltonian in the envelope approximation,[63–66] where the residual strain is found by minimizing the elastic energy in the structure. The explicit form of the kinetic and strain Hamiltonians are given in Ref. 64. Multiparticle states are calculated within the Hartree approximation, in which the wave functions are found by iteratively solving the Schrödinger equation for a particle in the potential of the other carriers in the QD until the energy eigenvalues converge. The Hartree approach accounts for the direct Coulomb interaction between the carriers, but does not capture the exchange interaction or the effects of correlation. The fine-structure splitting is therefore introduced by hand. We take a value of 150 μeV, which is typical of values found in experiment.[58] We find that the exact value of δ is

TABLE I. Transition energies and electric dipole moments calculated using eight-band, strain-dependent $\boldsymbol{k}\cdot\boldsymbol{p}$ theory. An empirical value was used for the fine-structure splitting (Ref. 58).

Parameter	Value
Exciton transition energy ($E_{00,10}$)	1.2723 eV
Biexciton transition energy ($E_{10,11}$)	1.2739 eV
Binding energy (Δ_b)	−1.6 meV
Fine-structure splitting (δ)	150 μeV
Dipole moment ($d_{00,10}$)	22.76 Debye
Dipole moment ($d_{01,11}$)	22.98 Debye

inconsequential due to the fast time scale of the optical control process relative to $1/\delta$. The matrix elements of the electric dipole operator are directly evaluated using the calculated multiparticle states. The biexciton binding energy is evaluated using the difference between the transition energies calculated using the multiparticle and single-particle wave functions. The results of our electronic structure calculations are summarized in Table I.

The biexciton binding energy is a crucial parameter for the design of optical control pulses for both the single-qubit and C-ROT gates as it determines the relative spacing of the optical transitions involved. A small value of Δ_b will require fine spectral control of the pulse phase and amplitude. Experiments have shown that it is possible to get both negative (antibinding) and positive (binding) biexciton binding energies, with values of Δ_b ranging from 4.8 to −6.3 meV in self-assembled In(Ga)As QDs.[67] This wide range of experimental values illustrates the strong sensitivity of this parameter to the details of the QD structure and composition. This sensitivity is further illustrated by the results in Fig. 2, which show electronic structure calculations for a range of dot compositions and heights. Variations in the biexciton binding energy in Fig. 2 reflect changes in the overlap of the electron and hole wave functions. The average indium composition in Fig. 2(a) is varied by changing the maximum indium concentration at the top face of the dot while maintaining an identical graded structure and compositional gradient Δx as in Fig. 1(d). There is a nonmonotonic dependence on average indium composition, reflecting relative shifts in the electron and hole wave functions due to the nonuniform dot composition as the average indium content varies. The height of the dot in Fig. 2(b) is varied by adding horizontal layers to the top of the dot with a starting height of 2.5 nm while maintaining the same internal and external facet angles and spacing between layers. With this approach, material added to the top simultaneously increases the height and the average indium composition because the top face of the dot contains the indium-rich layers. (For a dot height of 4.5 nm, the average indium composition is 0.5.) The results in Fig. 2(b) reflect a tendency for the biexciton to become more tightly bound (smaller negative binding energies) with increasing dot height. As our calculations neglect correlation effects, we can only obtain qualitative information regarding the trends in Δ_b with QD structure (e.g., the value we extract for the biexciton binding energy is consistently negative due to the overestimation of the effects of electron-electron repulsion[68]). Nevertheless, these results suggest that Δ_b may be engineered through appropriate

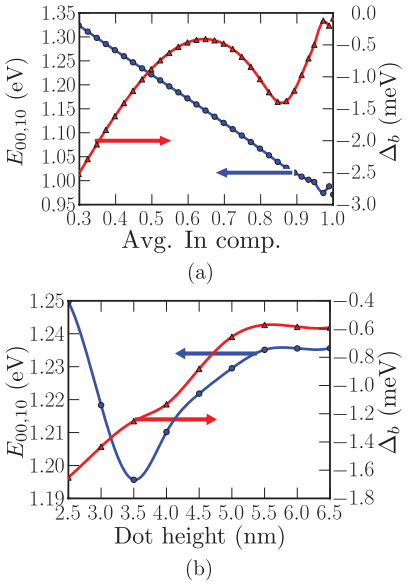

FIG. 2. (Color online) Exciton transition energy (circles) and biexciton binding energy (triangles) for variations in (a) average indium composition and (b) quantum dot height. In varying the dot height, material was added to the top of the dot [see Fig. 1(d)], while maintaining the same graded structure, until a complete pyramid was formed ($h = 6.5$ nm).

choice of growth conditions. This is consistent with recent experiments, in which Δ_b was tuned through control of the height of site-selected QDs.[69] The trends observed in Fig. 2 for the exciton transition energy are determined by competition between changes in the dot compositional profile and the degree of quantum confinement. In the numerical simulations of the C-ROT gate, we have allowed the biexciton binding energy to vary, spanning the range of accessible experimental values.[67] This will allow us to obtain flexible pulse-shaping protocols that may be adapted to a particular QD during experimental implementation of the C-ROT gate.

IV. OPTIMIZATION OF THE C-ROT GATE

The interaction of a laser pulse with the QD is treated using the Liouville equation for the density matrix $\rho(t)$,

$$\frac{\partial\rho}{\partial t} = \frac{i}{\hbar}[\rho, H], \tag{1}$$

where H is the total Hamiltonian, given by

$$H = \sum_i \hbar\omega_i P_{i,i} - \frac{1}{2}\sum_{i\neq j}\boldsymbol{\mu}_{i,j}\cdot\hat{\boldsymbol{\epsilon}}E_0(t) \times\{\exp[-i\omega t - i\Phi(t)] + \exp[i\omega t + i\Phi(t)]\}P_{i,j}. \tag{2}$$

The first term in Eq. (2) describes the electronic structure for the unperturbed system, consisting of the multiparticle eigenstates obtained using our $\boldsymbol{k}\cdot\boldsymbol{p}$ formalism, where $P_{i,j}$ is the associated projection operator $|i\rangle < j|$. The second term is the control Hamiltonian associated with the laser field. We employ the rotating-wave approximation to remove the nonresonant term in the interaction Hamiltonian and make the change of variables $\rho_{i,j}(t) \rightarrow \tilde{\rho}_{i,j}(t)$ to remove the

fast variations in the coherences. Decay and decoherence are incorporated in the relaxation-time approximation. The resulting Bloch equations of the four-level system are given by

$$
\begin{aligned}
\dot{\tilde{\rho}}_{01,01} &= -\frac{i}{2}(\chi_{01,00}\tilde{\rho}_{00,01} - \chi_{00,01}\tilde{\rho}_{01,00} + \chi_{01,11}\tilde{\rho}_{11,01} - \chi_{11,01}\tilde{\rho}_{01,11}) - \gamma_{01,01}\tilde{\rho}_{01,01},\\
\dot{\tilde{\rho}}_{10,10} &= -\frac{i}{2}(\chi_{10,00}\tilde{\rho}_{00,10} - \chi_{00,10}\tilde{\rho}_{10,00} + \chi_{10,11}\tilde{\rho}_{11,10} - \chi_{11,10}\tilde{\rho}_{10,11}) - \gamma_{10,10}\tilde{\rho}_{10,10},\\
\dot{\tilde{\rho}}_{11,11} &= -\frac{i}{2}(\chi_{11,01}\tilde{\rho}_{01,11} - \chi_{01,11}\tilde{\rho}_{11,01} + \chi_{11,10}\tilde{\rho}_{10,11} - \chi_{10,11}\tilde{\rho}_{11,10}) - \gamma_{11,11}\tilde{\rho}_{11,11},\\
\tilde{\rho}_{00,00} &= 1 - \tilde{\rho}_{01,01} - \tilde{\rho}_{10,10} - \tilde{\rho}_{11,11},\\
\dot{\tilde{\rho}}_{01,00} &= -\frac{i}{2}[2(\omega_{01,00} - \omega)\tilde{\rho}_{01,00} + \chi_{01,11}\tilde{\rho}_{11,00} - \chi_{10,00}\tilde{\rho}_{01,10} + \chi_{01,00}(\tilde{\rho}_{00,00} - \tilde{\rho}_{01,01})] - \gamma_{01,00}\tilde{\rho}_{01,00},\\
\dot{\tilde{\rho}}_{10,00} &= -\frac{i}{2}[2(\omega_{10,00} - \omega)\tilde{\rho}_{10,00} + \chi_{10,11}\tilde{\rho}_{11,00} - \chi_{01,00}\tilde{\rho}_{10,01} + \chi_{10,00}(\tilde{\rho}_{00,00} - \tilde{\rho}_{10,10})] - \gamma_{10,00}\tilde{\rho}_{10,00},\\
\dot{\tilde{\rho}}_{10,01} &= -\frac{i}{2}[2\omega_{10,01}\tilde{\rho}_{10,01} + \chi_{10,00}\tilde{\rho}_{00,01} - \chi_{00,01}\tilde{\rho}_{10,00} + \chi_{10,11}\tilde{\rho}_{11,01} - \chi_{11,01}\tilde{\rho}_{10,11}] - \gamma_{10,01}\tilde{\rho}_{10,01},\\
\dot{\tilde{\rho}}_{11,00} &= -\frac{i}{2}[2(\omega_{11,00} - 2\omega)\tilde{\rho}_{11,00} + \chi_{11,01}\tilde{\rho}_{01,00} - \chi_{01,00}\tilde{\rho}_{11,01} + \chi_{11,10}\tilde{\rho}_{10,00} - \chi_{10,00}\tilde{\rho}_{11,10}] - \gamma_{11,00}\tilde{\rho}_{11,00},\\
\dot{\tilde{\rho}}_{11,01} &= -\frac{i}{2}[2(\omega_{11,01} - \omega)\tilde{\rho}_{11,01} + \chi_{11,10}\tilde{\rho}_{10,01} - \chi_{00,01}\tilde{\rho}_{11,00} + \chi_{11,01}(\tilde{\rho}_{01,01} - \tilde{\rho}_{11,11})] - \gamma_{11,01}\tilde{\rho}_{11,01},\\
\dot{\tilde{\rho}}_{11,10} &= -\frac{i}{2}[2(\omega_{11,10} - \omega)\tilde{\rho}_{11,10} + \chi_{11,01}\tilde{\rho}_{01,10} - \chi_{00,10}\tilde{\rho}_{11,00} + \chi_{11,10}(\tilde{\rho}_{10,10} - \tilde{\rho}_{11,11})] - \gamma_{11,10}\tilde{\rho}_{11,10},
\end{aligned}
\tag{3}
$$

where $\rho_{i,i}$ is the population in state $|i\rangle$, $\rho_{i,j}$ is the coherence between states $|i\rangle$ and $|j\rangle$, $\chi_{i,j} = \boldsymbol{\mu}_{i,j}\cdot\hat{\boldsymbol{\epsilon}}E_0(t)/\hbar$ is the Rabi frequency, and $\gamma_{i,j}$ are the constant decay rates.

The objective of quantum control is to tailor the control Hamiltonian to achieve the desired multiparticle state of the system at the end of the laser pulse. This can be achieved experimentally, for example, using a $4f$ pulse shaper,[29] as shown in Fig. 3. The manipulation of the pulse shape is carried out in the Fourier plane by a spatial light modulator (SLM), which may be equipped with one or two voltage-controlled liquid-crystal retarders. When two liquid-crystal retarders are used in conjunction with polarizers on the input and output of the SLM, full control of the amplitude and phase of the pulse is possible. The action of the SLM in this case may be described as the product of frequency-dependent amplitude $[A_M(\omega)]$ and phase $[\Phi_M(\omega)]$ masks:

$$M(\omega) = A_M(\omega)\exp[i\Phi_M(\omega)]. \tag{4}$$

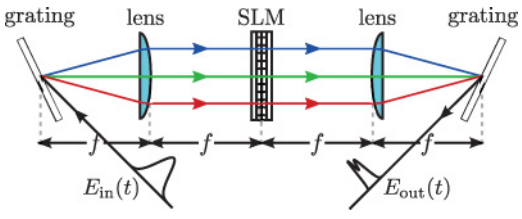

FIG. 3. (Color online) $4f$ pulse shaper consisting of two diffraction gratings, two lenses, and an optical mask shown as a spatial light modulator (SLM). The distance f is the focal length of the lenses. Manipulation of the pulse shape is carried out in the Fourier plane.

The effect of this mask on the pulse at the Fourier plane is given by

$$\tilde{E}_{\rm out}(\omega) = \tilde{E}_{\rm in}(\omega)M(\omega), \tag{5}$$

where $\tilde{E}_{\rm in}(\omega)$ is the Fourier transform of the input pulse, taken to be transform limited:

$$\boldsymbol{E}_{\rm in}(t) = \tfrac{1}{2}\hat{\boldsymbol{\epsilon}}E_0(t)\exp(-i\omega_0 t). \tag{6}$$

The pulse envelope is chosen to have the form $E_0(t) = |E_0|\mathrm{sech}(1.76t/\tau)$, with $\tau = 150$ fs, which is consistent with the typical output from commercially available femtosecond laser systems operating in the wavelength range of interest. $\tilde{E}_{\rm out}(\omega)$ is the Fourier transform of the output (shaped) pulse used for quantum control. Phase-only SLM configurations minimize light losses, and for this reason we develop pulse-shaping protocols involving phase-only control as well as amplitude-only control. This will provide the greatest degree of flexibility in the experimental implementation of the phase masks presented in Sec. IV A.

We optimize the phase and amplitude masks using the constrained optimization by linear approximations (COBYLA) algorithm.[70] The objective function to be maximized by the optimization routine is the fidelity of the quantum gate, given by

$$F = \mathrm{Tr}[\rho_{\rm P}\rho_{\rm I}], \tag{7}$$

where, $\rho_{\rm P}$ is the physical density matrix at the end of the laser pulse and $\rho_{\rm I}$ is the ideal density matrix.[25] Equation (7) is applied to the C-ROT operation by averaging the fidelity over four initial states, corresponding to an occupation of unity for each of the four levels in the system, with all other

density-matrix elements equal to zero. In this case, a pure initial system state is assumed; i.e., we do not model the quantum state initialization, assuming it to have been carried out with a fidelity of unity. The time dynamics of the system are calculated by integrating Eq. (3) over the duration of the pulse. We define the fidelity F as a function of a vector $\boldsymbol{q}$, the components of which describe the mask function $M(\omega)$, such that

$$F = f(q_1, \ldots, q_i, \ldots, q_n). \tag{8}$$

The components of the vector $\boldsymbol{q}$ are subject to constraints dictated by experimental limitations, as described below for each shaping scheme. We use a Sobol' sequence[71,72] to populate the n-dimensional parameter space with initial vectors $\{\boldsymbol{q}_{\text{init}}\}$, each describing different forms of the masking function, $M(\omega)$. For each vector, Eq. (3) is integrated to determine the density matrix at the end of the laser pulse, and this density matrix is inserted into Eq. (7) to calculate the fidelity. The optimization routine drives the system to a local optimum in fidelity by varying the components of $\boldsymbol{q}$. We find that the optimal solution is found uniquely for a population of 500 (or more) initial vectors, indicating that the parameter space is adequately spanned for each shaping scheme.

A. Phase control scheme

A scheme for quantum control in which the only degree of freedom is the phase of the pulse offers some advantages: (i) light losses in the shaping system will be minimized and (ii) such a system avoids deleterious effects associated with rejected light in the shaping system. The phase mask we utilize here has the following dependence on the individual frequencies ω within the pulse:

$$\Phi_M(\omega) = \alpha \cos[\gamma(\omega - \omega_{10,11}) - \delta]. \tag{9}$$

Here $\omega_{10,11}$ is the transition frequency resonant with the $|10\rangle \rightarrow |11\rangle$ transition, and α, γ, δ, and the total pulse area $[\Theta = (\boldsymbol{\mu} \cdot \hat{\boldsymbol{\epsilon}}/\hbar) \int_{-\infty}^{+\infty} E_0(t)\, dt]$ are taken as free parameters, so that the fidelity is a function of four variables:

$$F = f(\alpha, \gamma, \delta, \Theta). \tag{10}$$

The following constraints are imposed:

$$\begin{aligned} 0 &\leqslant \alpha \leqslant \pi, \\ 0 &\leqslant \gamma \leqslant 315 \text{ fs}, \\ -\pi &\leqslant \delta \leqslant \pi, \\ \pi/2 &\leqslant \Theta \leqslant 6\pi. \end{aligned} \tag{11}$$

The limits on α and γ were chosen to restrict $|d\Phi_M(\omega)/d\omega|_{\max}$ to approximately $\pi/10$ radians per pixel for a 128-pixel SLM, representing a readily accessible phase gradient for typical pulse-shaping systems. Θ was allowed to vary up to 6π radians as it was found that multiple Rabi oscillation cycles provided access to higher fidelities, as discussed in Sec. V. 6π radians is considered to be a good compromise for achieving high fidelities with experimentally accessible pulse fluences.[73]

B. Amplitude control scheme

The amplitude mask function we employ here has the following form:

$$A_M(\omega) = \left| \exp\left[-\left(\frac{\omega - \omega_{10,11}}{\Delta\omega_1/(2 \ln 2)^{1/2}} \right)^2 \right] - A_0 \exp\left[-\left(\frac{\omega - \omega_{00,10}}{\Delta\omega_2/(2 \ln 2)^{1/2}} \right)^2 \right] \right|. \tag{12}$$

Equation (12) represents the destructive interference of simultaneous bichromatic Gaussian pulses centered at photon energies $E_{10,11} = \hbar\omega_{10,11}$ and $E_{00,01} = \hbar\omega_{00,01}$, with full width at half maximum frequency bandwidths $\Delta\omega_i$, and a relative amplitude factor A_0. For simplicity, we set $\Phi_M(\omega)$ in Eq. (4) equal to zero. The analytical form in Eq. (12) was inspired by the results in Ref. 6, in which a similar four-level system was considered, and the C-ROT gate was optimized by separately controlling the pulse durations of two phase-locked Gaussian pulses. The amplitude mask in Eq. (12) is a more general form and is easily implemented using a single mode-locked oscillator and a commercial pulse shaper.

The fidelity is maximized in a four-dimensional parameter space:

$$F = f(\Delta\omega_1, \Delta\omega_2, A_0, \Theta). \tag{13}$$

The free parameters $\Delta\omega_i$, A_0, and Θ are subject to the following constraints:

$$\begin{aligned} 6.08 &\leqslant \hbar\Delta\omega_i \leqslant 12.2 \text{ meV}, \\ 0.0 &\leqslant A_0 \leqslant 1.0, \\ \pi/2 &\leqslant \Theta \leqslant 6\pi. \end{aligned} \tag{14}$$

The maximum limit on the bandwidths $\Delta\omega_i$ is determined by the spectral content of the initial transform-limited optical pulse, while the minimum limit restricts the total pulse operation time. The restrictions on Θ were kept the same as for the phase control scheme, so that the effectiveness of the two schemes could be compared. It should be noted that it is not possible to enforce a constant maximum rate of change, $|dA_M(\omega)/d\omega|_{\max}$, for all binding energies. We nevertheless verified that the spectral amplitude features obtained for the optimal pulse shapes are sufficiently slowly varying to be well reproduced by a standard 128-pixel SLM.

V. RESULTS AND DISCUSSION

A. Optimized quantum control pulses

Figure 4 shows the results for the optimum pulse shape using the phase-only control scheme for a biexciton binding energy of 2.5 meV. In order to quantify the efficacy of the pulse-shaping protocols presented in this work, we compare the gate performance for the shaped pulse to that for a TL pulse with an equivalent gate time. The optimized parameters for the shaped pulse are $\alpha = 0.511\ \pi$ rad, $\gamma = 325$ fs, $\delta = 0.243\ \pi$ rad, and $\Theta = 5.780\ \pi$ rad. These data correspond to a gate time of 555 fs for the TL and shaped pulses. The population dynamics are shown in the two upper panels in Fig. 4 for two initial conditions: (i) $\rho_{10,10}(t = 0) = 1$ and

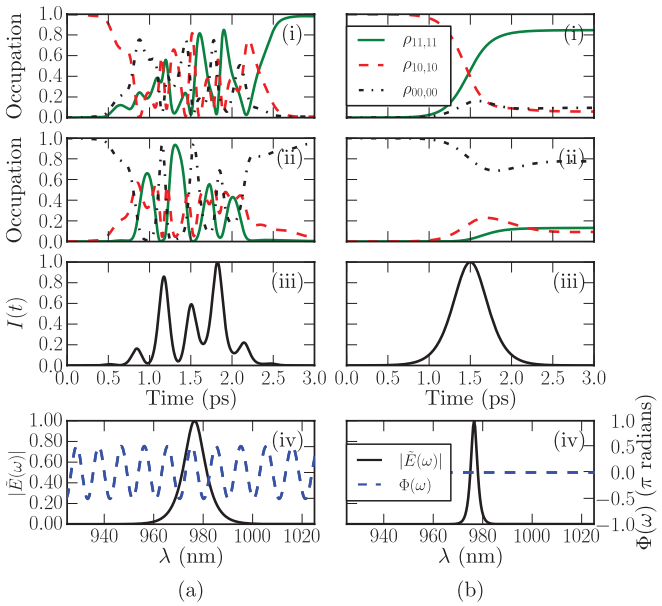

FIG. 4. (Color online) Population dynamics and control pulse characteristics for (a) the optimal phase-shaped pulse and (b) the TL pulse. Panels (i) and (ii) show the population dynamics for the initial conditions $\rho_{10,10}(t=0)=1$ and $\rho_{00,00}(t=0)=1$, respectively. The third panel shows the temporal envelope of the electric-field intensity of the control pulse. The bottom panel shows the amplitude (solid curves) and phase (dashed curves) profiles for the control pulse.

(ii) $\rho_{00,00}(t=0)=1$. As discussed in Sec. II, the objective of the C-ROT gate is to flip the state of the target (second) bit if and only if the control (first) bit is 1. This implies that the optical pulse should effect a π Rabi rotation between $|10\rangle$ and $|11\rangle$ if the system is initially in either $|10\rangle$ or $|11\rangle$ and have no effect if the system is in $|00\rangle$ or $|01\rangle$ at $t=0$.

For $\rho_{10,10}(t=0)=1$ (top row of panels in Fig. 4) the first bit is 1 at time $t=0$. In this case, the C-ROT gate must flip the second bit so that the occupation $\rho_{11,11}=1$ at the end of the pulse. As seen in Fig. 4(a), the shaped pulse carries out this operation with a high fidelity. The occupations $\rho_{11,11}$ and $\rho_{10,10}$ are flipped such that $\rho_{11,11}$ starts at 0 and ends at approximately 1, while $\rho_{10,10}$ starts at 1 and ends at approximately 0. The occupation for the nontarget state ($\rho_{00,00}$) starts at 0 and after some transient occupation is returned to approximately 0. For the TL pulse in Fig. 4(b), an incomplete transfer of occupation between $\rho_{10,10}$ and $\rho_{11,11}$ occurs and the residual occupation in $\rho_{00,00}$ is nonzero, resulting in lower fidelity.

For the second initial condition, $\rho_{00,00}(t=0)=1$ (second row of panels in Fig. 4), the first bit is 0 at $t=0$, so an ideal pulse would return the system to its initial state. The shaped pulse is also able to perform this operation with high fidelity as seen in Fig. 4(a). The occupations $\rho_{11,11}$ and $\rho_{10,10}$ start at 0 at time $t=0$ and both are returned to approximately 0 after some transient dynamics. Additionally, the occupation in $\rho_{00,00}$ starts at 1 and is returned to 1. The TL pulse is ineffective for this operation as it permanently reduces the occupation $\rho_{00,00}$, resulting in residual values of the occupations $\rho_{11,11}$ and $\rho_{10,10}$ at the end of the pulse. The state evolution for the initial condition $\rho_{11,11}(t=0)=1$ is linked to the evolution for $\rho_{10,10}(t=0)=1$ as these state occupations are exchanged in the C-ROT and so only the dynamics for $\rho_{10,10}(t=0)=1$ are shown for clarity. The optical selection rules for a Π_y-polarized pulse preclude laser-induced dynamics for the fourth initial condition $\rho_{01,01}(t=0)=1$ [see Fig. 1(a)].

The temporal and spectral properties of the shaped and TL control laser pulses are shown in the two lower panels of Fig. 4. The TL pulse with an equivalent gate time has a narrower frequency spectrum than the shaped pulse and a constant phase. The sinusoidal phase modulation for the shaped pulse results in a structured intensity profile and concomitant intermediate state dynamics. The improvement in fidelity afforded by the shaping protocol is nevertheless considerable, reaching a value of 0.964 in comparison to 0.866 for the TL pulse.

An alternative view of the state dynamics is provided by the Bloch vector representation, shown in Figs. 5(a) and 5(b) for the phase-shaped and TL pulses, respectively. The solid line indicates the Bloch vector corresponding to the first qubit for $\rho_{00,00}(t=0)=1$, while the dashed curve corresponds to the second qubit for $\rho_{10,10}(t=0)=1$. The complex trajectories in Fig. 5(a) reflect the intermediate state dynamics in Fig. 4(a).

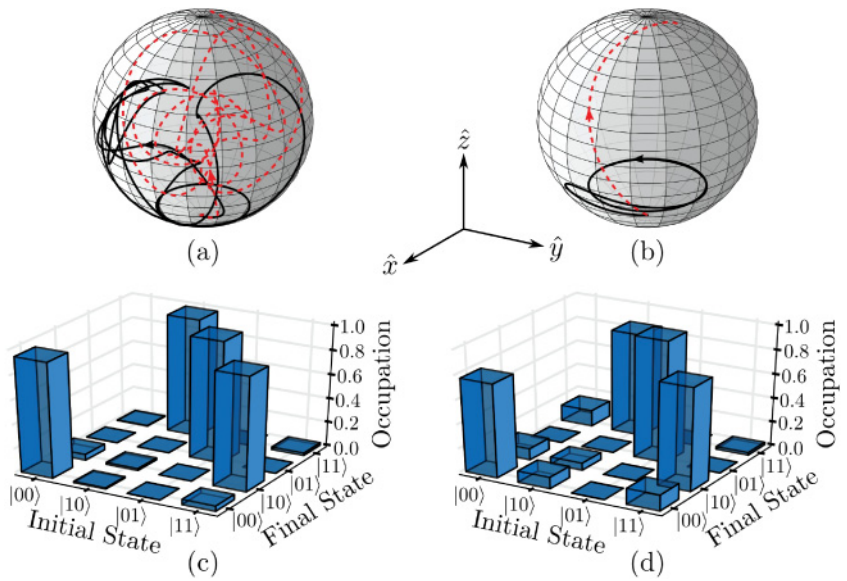

FIG. 5. (Color online) Bloch vector representations of the first qubit for $\rho_{00,00}(t=0)=1$ (solid curve) and the second qubit for $\rho_{10,10}(t=0)=1$ (dashed curve) for the (a) phase-shaped pulses and (b) TL pulse. Truth table of the gate operation for the (c) optimal phase-shaped pulse and (d) TL pulse.

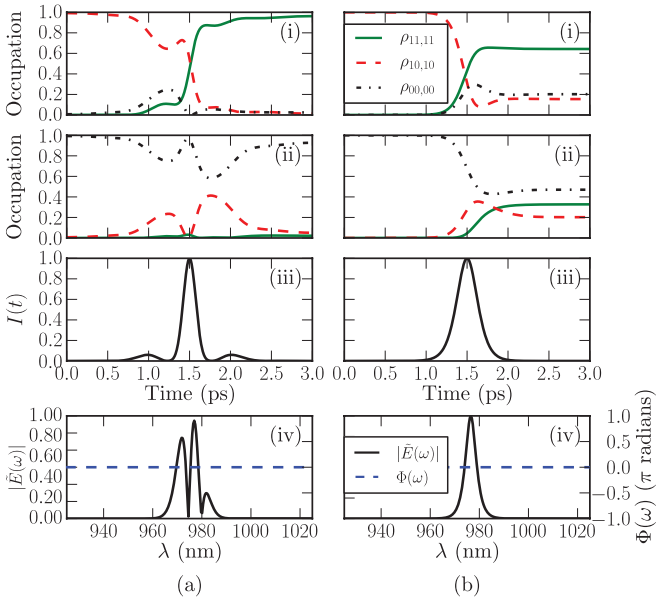

FIG. 6. (Color online) Population dynamics and control pulse characteristics for (a) the optimal amplitude-shaped pulse and (b) the TL pulse. Panels (i) and (ii) show the population dynamics for the initial conditions $\rho_{10,10}(t=0)=1$ and $\rho_{00,00}(t=0)=1$, respectively. The third panel shows the temporal envelope of the electric-field intensity of the control pulse. The bottom panel shows the amplitude (solid curves) and phase (dashed curves) profiles for the control pulse.

The increased efficacy of the C-ROT operation for the phase-shaped pulse is evident in Fig. 5(a) as the second qubit undergoes a half-cycle rotation for $\rho_{10,10}(t=0)=1$ (dashed curves), while the first qubit is returned to the initial state for $\rho_{00,00}(t=0)=1$ (solid curves). The higher fidelity obtained with the phase-shaping protocol relative to the TL pulse is also illustrated by the truth tables in Figs. 5(c) and 5(d). The TL pulse leads to inferior control of the conditional dynamics because the wide spectral bandwidth relative to Δ_b prevents discrimination between the target and nontarget states in the optical excitation process.

Figure 6 shows the results for the optimal amplitude-shaped pulse for the same binding energy of 2.5 meV. The optimized parameters for the shaped pulse are $\hbar\Delta\omega_1 = 6.083$ meV, $\hbar\Delta\omega_2 = 12.166$ meV, $A_0 = 0.772$, and $\Theta = 3.6\,\pi$ rad. The gate time for the data in Fig. 6 is 335.5 fs for both shaped and TL pulses. The Bloch vector and truth table results corresponding to the state dynamics in Fig. 6 are shown in Fig. 7. The fidelity of the C-ROT gate for the amplitude-shaped pulse is 0.967, in comparison with a value of 0.689 for the TL pulse, illustrating a dramatic improvement with pulse shaping.

The amplitude mask in Eq. (12) is a superposition of two Gaussians that are π out of phase with each other. From the bottom panel in Fig. 6, it is clear that the optimum condition for high fidelity corresponds to the generation of a node in the pulse spectrum resonant with the $|00\rangle \rightarrow |10\rangle$ transition (occurring at 974.5 nm). The optimum pulse parameters therefore result in perfect destructive interference between the two terms in Eq. (12) at $\omega = \omega_{00,10}$. Such a cancellation effect was also found in Ref. 6 for a similar four-level scheme involving pure exciton spin states in cylindrically symmetric quantum dots. Our results for the level scheme in Fig. 1(a), for which the ground state is coupled to the biexciton via the intermediate state $|01\rangle$, and for which our more general amplitude mask in Eq. (12) permits relative amplitude control between the two terms, indicates that the cancellation effect is a general consequence of the use of this bichromatic control scheme. As described in the next section, our findings also verify that the spectral node tracks the $|00\rangle \rightarrow |10\rangle$ transition as Δ_b is varied. (In Ref. 6 Δ_b was fixed.) Unlike the amplitude-shaping scheme, for which there exists a simple interpretation of the improvement in fidelity introduced by pulse shaping in terms of destructive light interference at $\omega_{00,10}$, for the phase-only shaping protocol the pulse spectrum is unaffected by the shaping mask and consequently no such simple interpretation exists. In contrast to the case of a TL pulse, in which the Rabi rotation on the Bloch sphere occurs about a fixed axis in the x-y plane, the introduction of a time- (and frequency-) dependent phase in the control pulse will lead to the motion of the Rabi control vector during the operation. In conjunction with the freedom to perform more

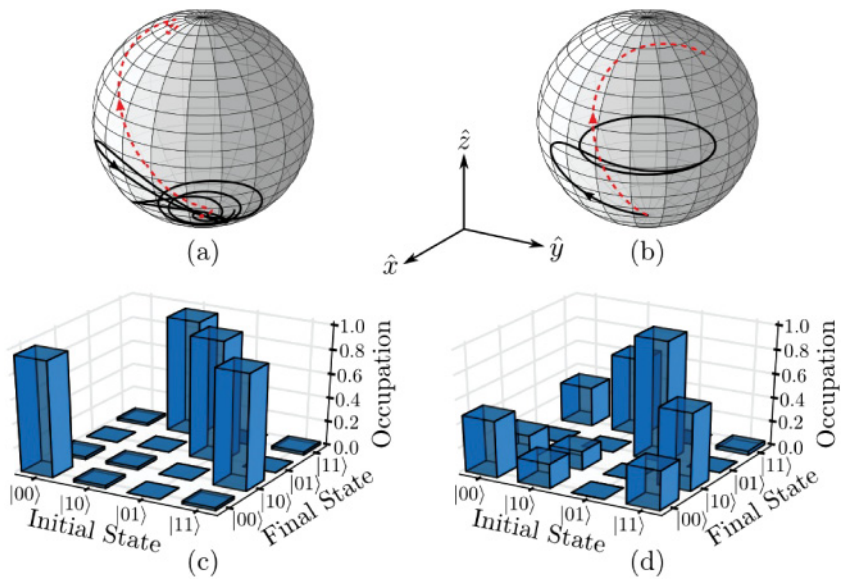

FIG. 7. (Color online) Bloch vector representations of the first qubit for $\rho_{00,00}(t=0)=1$ (solid curve) and the second qubit for $\rho_{10,10}(t=0)=1$ (dashed curve) for the (a) amplitude-shaped pulses and (b) TL pulse. Truth table of the gate operation for the (c) optimal amplitude-shaped pulse and (d) TL pulse.

than one full Rabi cycle in our shaping protocol, this leads to a complex motion of the Bloch vector, as evident in Fig. 5(a). Optimization of the fidelity only requires that the system reach the target state *at the end of the control pulse*. The phase-only shaping scheme used in Eq. (9) was chosen for its simplicity of implementation and for the ease of monitoring the control pulses using common pulse measurement techniques. We expect that another choice of phase mask function would lead to similar improvements in fidelity provided sufficiently rapid phase variations may be generated within the experimental constraints of conventional SLMs. The ability to tailor the coherent state dynamics using only control over the pulse phase, illustrated here for exciton qubits in self-assembled quantum dots, highlights the power and flexibility of pulse shaping in tailoring the light-matter interaction.

B. Dependence on biexciton binding energy

The variation of the fidelity and gate time with the size of the binding energy of the biexciton is shown in Fig. 8 for the optimum-shaped and TL pulses. The gate fidelity is independent of the sign of Δ_b, indicating that only the magnitude of the energy separation between the $|00\rangle \rightarrow |10\rangle$ and $|10\rangle \rightarrow |11\rangle$ transitions is important. The phase- and amplitude-shaped pulses outperform the TL pulses for the full range of binding energies investigated. The pulse parameters corresponding to the data in Fig. 8 are shown in Tables II and III for the phase- and amplitude-shaping protocols, respectively. The pulse parameters for positive and negative binding energies were found to be similar, and so only the trends for positive binding energies are provided. For the phase-shaped pulses,

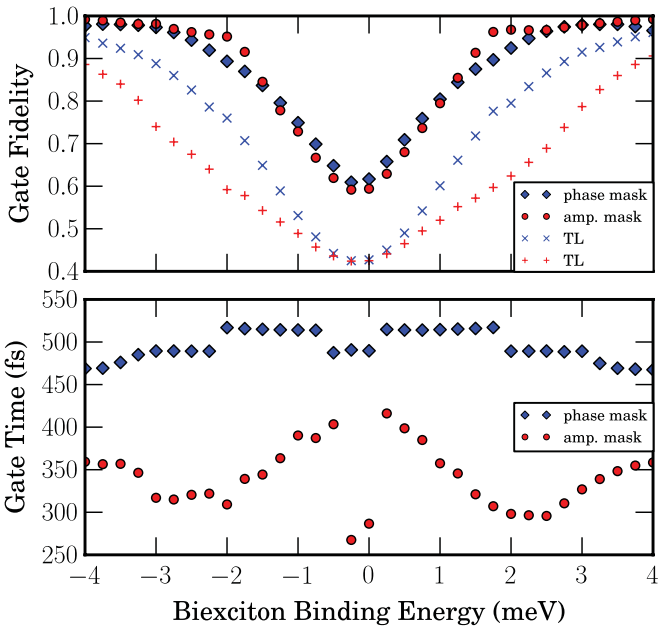

FIG. 8. (Color online) (Top) Fidelity for the optimal phase-shaped pulses (diamonds) and optimal amplitude-shaped pulses (circles) is shown as a function of the biexciton binding energy. The fidelities of the corresponding TL pulses with equivalent gate times are also shown for the phase-shaped pulses (×) and amplitude-shaped pulses (+). (Bottom) Gate time of optimal phase-shaped (diamonds) and amplitude-shaped (circles) pulses as a function of binding energy.

TABLE II. The optimum pulse parameters obtained for the phase-shaping protocol for a range of values of the biexciton binding energy. The resulting C-ROT gate time (GT) is also shown.

Δ_b (meV)	F	α (π rad)	γ (fs)	δ (π rad)	Θ (π rad)	GT (fs)
0.00	0.617	0.460	325.0	−0.770	3.617	555.7
0.25	0.658	0.600	325.0	0.854	5.841	584.1
0.50	0.709	0.602	325.0	0.841	5.769	583.3
0.75	0.759	0.603	325.0	−0.165	5.759	583.2
1.00	0.805	0.606	325.0	0.832	5.758	583.8
1.25	0.844	0.608	325.0	−0.168	5.765	584.5
1.50	0.875	0.610	325.0	0.832	5.759	585.3
1.75	0.897	0.613	325.0	−0.165	5.771	586.7
2.00	0.925	0.507	325.0	−0.758	5.775	555.0
2.25	0.947	0.509	325.0	−0.757	5.779	555.2
2.50	0.964	0.511	325.0	0.243	5.780	555.3
2.75	0.974	0.513	323.3	−0.758	5.790	554.2
3.00	0.979	0.514	324.5	0.245	5.782	489.2
3.25	0.980	0.522	301.6	0.218	5.945	555.0
3.50	0.980	0.525	293.1	−0.791	6.000	532.4
3.75	0.975	0.526	291.2	−0.794	6.000	531.1
4.00	0.966	0.527	289.9	−0.796	6.000	530.3

the decrease in the sinusoidal amplitude α and frequency γ with increasing Δ_b in Table II occurs because less rapid changes in the phase are required for a high-fidelity operation between increasingly distant transitions. The phase δ, while having a critical influence on the temporal pulse profile and the resulting dynamics, does not have a discernible trend. We observe that $\Theta > \pi$ in all cases, indicating that the target quantum state is reached after multiple cycles of the Bloch vector. As Δ_b increases, the pulse center frequency tracks the $|10\rangle \rightarrow |11\rangle$ transition, and therefore the pulse energy at the $|00\rangle \rightarrow |10\rangle$ transition decreases. A greater overall pulse energy is then needed to reach the desired final state for all initial conditions simultaneously, leading to the increase in Θ with Δ_b in Table II. Our calculations indicate that further increasing the binding energy to values that are larger than the pulse bandwidth causes the optimum value of the pulse area to decrease toward π radians (e.g., $\Theta = 4.44\pi$ for $\Delta_b = 12$ meV and $\Theta = \pi$ for $\Delta_b = 24$ meV), as expected because in this trivial limit the undesired transition is not coupled to the laser field. We note that the meaning of the optimized pulse parameters are questionable for $\Delta_b \approx 0$, likely accounting for the two anomalous points around $\Delta_b = 0$ in the results for the amplitude mask in Fig. 8.

As seen in Table III, the amplitude-shaping protocol is ineffective for small Δ_b. The fidelity nevertheless increases rapidly as the separation between the transitions increases: A fidelity near unity is already achieved for $\Delta_b > 1.5$ meV. The bandwidth of the first Gaussian function is nearly constant at the lower limit of the imposed constraint because a narrow function maximizes the fraction of light contributing to the $|10\rangle \rightarrow |11\rangle$ Rabi rotation. In contrast, the bandwidth of the second term increases to its maximum value as Δ_b increases. A large value for $\hbar\Delta\omega_2$ maximizes the overlap of the pulse bandwidth of the second pulse with that of the first pulse. However, it is not clear why this overlap is advantageous for increasing the fidelity. The optimum values

TABLE III. The optimum pulse parameters obtained for the amplitude-shaping protocol for a range of values of the biexciton binding energy. The resulting C-ROT gate time (GT) is also shown.

Δ_b (meV)	F	$\hbar\Delta\omega_1$ (meV)	$\hbar\Delta\omega_2$ (meV)	A_0	Θ (π rad)	GT (fs)
0.00	0.594	6.967	9.428	0.902	5.843	325.2
0.25	0.629	6.099	6.458	0.898	5.889	472.1
0.50	0.680	6.083	6.744	0.899	6.000	452.3
0.75	0.737	6.083	7.085	0.900	6.000	436.7
1.00	0.795	6.083	7.572	0.902	6.000	405.7
1.25	0.855	6.083	8.340	0.900	6.000	392.1
1.50	0.913	6.083	9.780	0.897	6.000	364.4
1.75	0.962	6.190	11.121	0.885	6.000	348.5
2.00	0.968	6.083	11.991	0.850	5.029	338.2
2.25	0.966	6.083	12.166	0.815	4.318	336.4
2.50	0.967	6.083	12.166	0.772	3.600	335.5
2.75	0.973	6.083	12.166	0.728	3.048	352.3
3.00	0.979	6.083	12.166	0.685	2.683	370.9
3.25	0.983	6.083	12.166	0.643	2.400	384.7
3.50	0.986	6.083	12.166	0.603	2.175	395.2
3.75	0.990	6.083	12.166	0.566	1.998	402.7
4.00	0.992	6.083	12.166	0.530	1.857	406.7

for A_0 in Table III ensure that destructive interference at the $|10\rangle \rightarrow |11\rangle$ transition is complete. The pulse area Θ decreases monotonically with Δ_b in Table III, reflecting the relaxed requirements for high-fidelity operation. This reduction in Θ also leads to a decrease in the fraction of light reflected by the pulse shaper in imposing the amplitude-shaping scheme.

It should be noted that the amplitude-shaping protocol provides shorter gate times (by $\sim$30% on average) than the phase-shaping protocol, while the phase-shaping scheme avoids the deleterious effects associated with the rejected light in the pulse shaper. As only two shaping schemes are investigated here, it is reasonable to expect a further improvement in the overall gate characteristics with the generalization of the shaping protocol to include simultaneous control over the amplitude and phase of the pulse. Improvements in gate performance may also be achieved using phase-only control schemes with a more complex choice for the phase mask function than that used here. The simple shaping schemes we have implemented serve to illustrate the power and flexibility of the pulse-shaping approach in achieving rapid, high-fidelity quantum operations on qubits in semiconductor quantum dots.

C. Inclusion of relaxation effects

The effects of dephasing were examined by introducing relaxation to the model, as discussed in Sec. IV. The population decay constants are set to values that are typical of $In_xGa_{1-x}As$ dots:[76] $T_1 = 480$ ps for the exciton states $|01\rangle$ and $|10\rangle$, and $T_1 = 320$ ps for the biexciton state $|11\rangle$ (i.e., $\gamma_{01,01} = \gamma_{10,10} = T_1^{-1}$ for the single excitons and $\gamma_{11,11} = T_1^{-1}$ for the biexciton). As described in Sec. IV, these effects are incorporated in the relaxation-time approximation. The longitudinal decay times are held fixed, while the T_2 times (γ_{ij}^{-1} for $i \neq j$) are taken to be the same for both exciton and biexciton states and are varied over a wide range up to the radiatively limited case. The fidelity was calculated by integrating Eq. (3) over 8 ps, with the pulse arriving at the center of the temporal window.

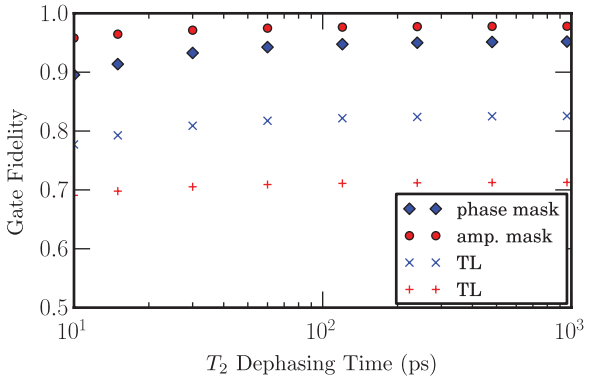

FIG. 9. (Color online) Fidelity versus dephasing time T_2 for the optimal phase-shaped pulses (diamonds) and optimal amplitude-shaped pulses (circles), and the TL sech pulses with gate time equivalent to that of the phase-shaped pulses ($\times$) and amplitude-shaped pulses ($+$).

The results of these calculations are shown in Fig. 9. We find that dephasing has only a small impact on the fidelity in all cases, even down to the shortest decoherence time considered (10 ps). This reflects the rapid nature of the C-ROT gate when ultrafast optical pulses are used. The impact of dephasing depends only on the gate time, giving a reduction of 6% for the phase-shaping scheme and 3% for the amplitude-shaping scheme with a dephasing time of 10 ps. Dephasing times for exciton qubits in semiconductor quantum dots in the range of several hundred picoseconds have been measured experimentally at low temperature.[77] In conjunction with the implementation of dynamical decoupling schemes for mitigating decoherence between gate operations,[51–53] these results indicate the feasibility of high-fidelity quantum computing using subpicosecond optical gates and semiconductor quantum dots.

VI. CONCLUSIONS

In conclusion, we have studied the use of pulse-shaping protocols that can be easily implemented using commercially available femtosecond laser systems and pulse shapers. We demonstrated the use of these protocols for the C-ROT gate in a realistic In(Ga)As quantum dot with electronic structure obtained using eight-band, strain-dependent $\boldsymbol{k}\cdot\boldsymbol{p}$ theory. Our results show that engineering the pulse using simple amplitude-only and phase-only shaping schemes provides considerable improvements in fidelity over a transform-limited pulse with the same operation time. The power and flexibility of pulse-shaping systems, which provide independent control of the pulse amplitude and phase, may be exploited to obtain further improvements in gate performance through generalization to more complex shaping schemes. The introduction of relaxation to the model was found to have a minimal effect on the gate fidelity for experimentally relevant dephasing times, reflecting the advantages of femtosecond optical pulses for quantum operations. Our results lay the groundwork for implementing pulse shaping in other quantum control processes, including two-photon Rabi rotations, adiabatic passage, and schemes for dynamical decoupling.

ACKNOWLEDGMENTS

This research is supported by the Canada Foundation for Innovation, the Natural Sciences and Engineering Research Council of Canada, Lockheed Martin Corporation, Rockwell Collins, the Canada Research Chairs Program, and DARPA.

[1] A. J. Ramsay, Semicond. Sci. Technol. **25**, 103001 (2010).
[2] D. Gammon, E. S. Snow, B. V. Shanabrook, D. S. Katzer, and D. Park, Science **273**, 87 (1996).
[3] D. Loss and D. P. DiVincenzo, Phys. Rev. A **57**, 120 (1998).
[4] E. Biolatti, R. C. Iotti, P. Zanardi, and F. Rossi, Phys. Rev. Lett. **85**, 5647 (2000).
[5] F. Troiani, U. Hohenester, and E. Molinari, Phys. Rev. B **62**, R2263 (2000).
[6] P. Chen, C. Piermarocchi, and L. J. Sham, Phys. Rev. Lett. **87**, 067401 (2001).
[7] J. H. Reina, L. Quiroga, and N. F. Johnson, Phys. Rev. A **62**, 012305 (2000).
[8] C. Piermarocchi, P. Chen, Y. S. Dale, and L. J. Sham, Phys. Rev. B **65**, 075307 (2002).
[9] A. Imamoğlu, D. D. Awschalom, G. Burkard, D. P. DiVincenzo, D. Loss, M. Sherwin, and A. Small, Phys. Rev. Lett. **83**, 4204 (1999).
[10] C. Piermarocchi, P. Chen, L. J. Sham, and D. G. Steel, Phys. Rev. Lett. **89**, 167402 (2002).
[11] F. Troiani, E. Molinari, and U. Hohenester, Phys. Rev. Lett. **90**, 206802 (2003).
[12] S. E. Economou, L. J. Sham, Y. Wu, and D. G. Steel, Phys. Rev. B **74**, 205415 (2006).
[13] S. M. Clark, K.-M. C. Fu, T. D. Ladd, and Y. Yamamoto, Phys. Rev. Lett. **99**, 040501 (2007).
[14] T. H. Stievater, X. Li, D. G. Steel, D. Gammon, D. S. Katzer, D. Park, C. Piermarocchi, and L. J. Sham, Phys. Rev. Lett. **87**, 133603 (2001).
[15] A. Zrenner, E. Beham, S. Stufler, F. Findeis, M. Bichler, and G. Abstreiter, Nature (London) **418**, 612 (2002).
[16] H. Kamada, H. Gotoh, J. Temmyo, T. Takagahara, and H. Ando, Phys. Rev. Lett. **87**, 246401 (2001).
[17] H. Htoon, T. Takagahara, D. Kulik, O. Baklenov, A. L. Holmes, and C. K. Shih, Phys. Rev. Lett. **88**, 087401 (2002).
[18] P. Borri, W. Langbein, S. Schneider, U. Woggon, R. L. Sellin, D. Ouyang, and D. Bimberg, Phys. Rev. B **66**, 081306 (2002).
[19] T. Flissikowski, A. Betke, I. A. Akimov, and F. Henneberger, Phys. Rev. Lett. **92**, 227401 (2004).
[20] S. Stufler, P. Machnikowski, P. Ester, M. Bichler, V. M. Axt, T. Kuhn, and A. Zrenner, Phys. Rev. B **73**, 125304 (2006).
[21] D. Press, T. D. Ladd, B. Zhang, and Y. Yamamoto, Nature (London) **456**, 218 (2008).
[22] B. D. Gerardot, D. Brunner, P. A. Dalgarno, P. Ohberg, S. Seidl, M. Kroner, K. Karrai, N. G. Stoltz, P. M. Petroff, and R. J. Warburton, Nature (London) **451**, 441 (2008).
[23] Y. Wu, X. Li, L. M. Duan, D. G. Steel, and D. Gammon, Phys. Rev. Lett. **96**, 087402 (2006).
[24] E. Poem, O. Kenneth, Y. Kodriano, Y. Benny, S. Khatsevich, J. E. Avron, and D. Gershoni, Phys. Rev. Lett. **107**, 087401 (2011).
[25] X. Li, Y. Wu, D. Steel, D. Gammon, T. H. Stievater, D. S. Katzer, D. Park, C. Piermarocchi, and L. J. Sham, Science **301**, 809 (2003).
[26] S. J. Boyle, A. J. Ramsay, F. Bello, H. Y. Liu, M. Hopkinson, A. M. Fox, and M. S. Skolnick, Phys. Rev. B **78**, 075301 (2008).
[27] G. Chen, N. H. Bonadeo, D. G. Steel, D. Gammon, D. S. Katzer, D. Park, and L. J. Sham, Science **289**, 1906 (2000).
[28] A. E. Siegman, *Lasers* (University Science Books, Sausalito, California, 1986).
[29] A. M. Weiner, Rev. Sci. Instrum. **71**, 1929 (2000).
[30] D. Meshulach and Y. Silberberg, Nature (London) **396**, 239 (1998).
[31] S. Zhdanovich, E. A. Shapiro, M. Shapiro, J. W. Hepburn, and V. Milner, Phys. Rev. Lett. **100**, 103004 (2008).
[32] B. Broers, H. B. van Linden van den Heuvell, and L. D. Noordam, Phys. Rev. Lett. **69**, 2062 (1992).
[33] B. Chatel, J. Degert, S. Stock, and B. Girard, Phys. Rev. A **68**, 041402 (2003).
[34] S. Chelkowski, A. D. Bandrauk, and P. B. Corkum, Phys. Rev. Lett. **65**, 2355 (1990).
[35] J. S. Melinger, S. R. Gandhi, A. Hariharan, D. Goswami, and W. S. Warren, J. Chem. Phys. **101**, 6439 (1994).
[36] P. Brumer and M. Shapiro, Annu. Rev. Phys. Chem. **43**, 257 (1992).
[37] H. Rabitz, R. de Vivie-Riedle, M. Motzkus, and K. Kompa, Science **288**, 824 (2000).
[38] K.-J. Boller, A. Imamoglu, and S. E. Harris, Phys. Rev. Lett. **66**, 2593 (1991).
[39] J. E. Field, K. H. Hahn, and S. E. Harris, Phys. Rev. Lett. **67**, 3062 (1991).
[40] J. B. Watson, A. Sanpera, X. Chen, and K. Burnett, Phys. Rev. A **53**, R1962 (1996).
[41] M. Jain, H. Xia, G. Y. Yin, A. J. Merriam, and S. E. Harris, Phys. Rev. Lett. **77**, 4326 (1996).
[42] T. Rickes, J. P. Marangos, and T. Halfmann, Opt. Commun. **227**, 133 (2003).
[43] H. Y. Hui and R. B. Liu, Phys. Rev. B **78**, 155315 (2008).
[44] T. Calarco, A. Datta, P. Fedichev, E. Pazy, and P. Zoller, Phys. Rev. A **68**, 012310 (2003).
[45] Y. Wu, I. M. Piper, M. Ediger, P. Brereton, E. R. Schmidgall, P. R. Eastham, M. Hugues, M. Hopkinson, and R. T. Phillips, Phys. Rev. Lett. **106**, 067401 (2011).
[46] C.-M. Simon, T. Belhadj, B. Chatel, T. Amand, P. Renucci, A. Lemaitre, O. Krebs, P. A. Dalgarno, R. J. Warburton, X. Marie, and B. Urbaszek, Phys. Rev. Lett. **106**, 166801 (2011).
[47] A. Borzì, G. Stadler, and U. Hohenester, Phys. Rev. A **66**, 053811 (2002).
[48] R.-B. Liu, W. Yao, and L. J. Sham, Phys. Rev. B **72**, 081306 (2005).
[49] T. A. Brun and H. Wang, Phys. Rev. A **61**, 032307 (2000).
[50] L. Quiroga and N. F. Johnson, Phys. Rev. Lett. **83**, 2270 (1999).
[51] P. Karbach, S. Pasini, and G. S. Uhrig, Phys. Rev. A **78**, 022315 (2008).
[52] T. E. Hodgson, L. Viola, and I. D'Amico, Phys. Rev. B **78**, 165311 (2008).
[53] V. M. Axt, P. Machnikowski, and T. Kuhn, Phys. Rev. B **71**, 155305 (2005).
[54] See, e.g., the Silhouette ultrafast pulse shaper manufactured by Coherent Inc.
[55] T. M. Sweeney, C. Phelps, and H. Wang, Phys. Rev. B **84**, 075321 (2011).

[56]G. Chen, T. H. Stievater, E. T. Batteh, X. Li, D. G. Steel, D. Gammon, D. S. Katzer, D. Park, and L. J. Sham, Phys. Rev. Lett. **88**, 117901 (2002).
[57]A. Muller, Q. Q. Wang, P. Bianucci, C. K. Shih, and Q. K. Xue, Appl. Phys. Lett. **84**, 981 (2004).
[58]M. Bayer, A. Kuther, A. Forchel, A. Gorbunov, V. B. Timofeev, F. Schäfer, J. P. Reithmaier, T. L. Reinecke, and S. N. Walck, Phys. Rev. Lett. **82**, 1748 (1999).
[59]R. Seguin, A. Schliwa, S. Rodt, K. Pötschke, U. W. Pohl, and D. Bimberg, Phys. Rev. Lett. **95**, 257402 (2005).
[60]N. Liu, J. Tersoff, O. Baklenov, A. L. Holmes, and C. K. Shih, Phys. Rev. Lett. **84**, 334 (2000).
[61]D. M. Bruls, J. W. A. M. Vugs, P. M. Koenraad, H. W. M. Salemink, J. H. Wolter, M. Hopkinson, M. S. Skolnick, F. Long, and S. P. A. Gill, Appl. Phys. Lett. **81**, 1708 (2002).
[62]P. W. Fry, I. E. Itskevich, D. J. Mowbray, M. S. Skolnick, J. J. Finley, J. A. Barker, E. P. O'Reilly, L. R. Wilson, I. A. Larkin, P. A. Maksym, M. Hopkinson, M. Al-Khafaji, J. P. R. David, A. G. Cullis, G. Hill, and J. C. Clark, Phys. Rev. Lett. **84**, 733 (2000).
[63]T. B. Bahder, Phys. Rev. B **41**, 11992 (1990).
[64]C. Pryor, Phys. Rev. B **57**, 7190 (1998).
[65]M. Holm, M.-E. Pistol, and C. Pryor, J. Appl. Phys. **92**, 932 (2002).
[66]C. E. Pryor and M. E. Flatté, Phys. Rev. Lett. **91**, 257901 (2003).
[67]C. Dal Savio, K. Pierz, G. Ade, H. Danzebrink, E. Göbel, and A. Hangleiter, Appl. Phys. B **84**, 317 (2006).
[68]A. Schliwa and M. Winkelnkemper, *Semiconductor Nanostructures*, edited by D. Bimberg (Springer Verlag, Berlin, 2008), pp. 139–164.
[69]M. E. Reimer, D. Dalacu, P. J. Poole, and R. L. Williams, J. Phys.: Conf. Ser. **210**, 012019 (2010).
[70]S. Johnson, The NLopt Nonlinear-Optimization Package.
[71]I. M. Sobol', USSR Comput. Math. Math. Phys. **7**, 86 (1967).
[72]W. Press, *Numerical Recipes: The Art of Scientific Computing* (Cambridge University Press, Cambridge, England, 2007).
[73]A. J. Ramsay, T. M. Godden, S. J. Boyle, E. M. Gauger, A. Nazir, B. W. Lovett, A. M. Fox, and M. S. Skolnick, Phys. Rev. Lett. **105**, 177402 (2010).
[74]The gate time for a given excitation pulse was determined by normalizing the intensity profile and determining the width of a square pulse with the same total area.
[75]In a follow-up paper (A. Gamouras, R. Mathew, and K. C. Hall, unpublished) we describe the experimental characterization of pulse shapes using multiphoton intrapulse interference phase scan.
[76]C. Santori, G. S. Solomon, M. Pelton, and Y. Yamamoto, Phys. Rev. B **65**, 073310 (2002).
[77]P. Borri, W. Langbein, S. Schneider, U. Woggon, R. L. Sellin, D. Ouyang, and D. Bimberg, Phys. Rev. Lett. **87**, 157401 (2001).